

IMAGE MOSAIC BASED ON LOCAL GUIDANCE AND DARK CHANNEL PRIOR

CHONG ZHANG, FANG XU, DEJIANG WANG[✉], HE SUN

Changchun Institute of Optics, Fine Mechanics and Physics, Chinese Academy of Sciences, Changchun 130000 China

e-mail: chongzhang17@mials.jlu.edu.cn; xufang@ciomp.ac.cn; wangdj04@ciomp.ac.cn; sunhe_ciomp@163.com.

(Received June 21, 2024; revised March 14, 2025; accepted March 17, 2025)

ABSTRACT

Image mosaic is of significance in various areas such as object tracking and drone reconnaissance. Aiming at the problems of poor performance and high rate of false match in foggy images, an improved stitching method based on local guided KAZE and dark channel prior is proposed. First of all, the KAZE algorithm is utilized for rough feature matching. Secondly, a local fixed point asymptotic method is introduced to optimize the global objective and eliminate mismatched point pairs. Then, the warp images are obtained by the estimated transformation matrix. Thirdly, the compensation of color and luminance difference of the overlap is applied to the overall image, which improves the inhomogeneity of stitching image. Eventually, the final result is obtained by enhancing algorithm based on dark channel prior. The proposed algorithm is assessed through intuitive renderings and quantitative values. Furthermore, the proposed method is compared with other common stitching methods. The results reveal that the method proposed in this paper gives the best performance in terms of the magnitude of feature matching pairs, the mean absolute error (MAE), the root mean square error (RMSE) and the processing time.

Keywords: dark channel; image mosaic; KAZE; local guided.

INTRODUCTION

Image mosaic is the process of combining several images contained overlapped area from different imaging devices and perspectives into an image with higher resolution (Lin *et al.*, 2022; Wang *et al.*, 2020). Currently, mosaics is still a hot topic which is widely used in multiple fields such as ground reconnaissance, medical image analysis and criminal case investigation (Gómez-Reyes *et al.*, 2022; Nie *et al.*, 2022; Wan *et al.*, 2021). However, it still faces many challenges such as disparity, image distortion, ghosting, inhomogeneity and a series of issues (Pham *et al.*, 2021; Zhang *et al.*, 2022; Lin *et al.*, 2022). In addition, the blurred images due to environment and weather greatly increases the difficulty of stitching.

At present, researchers have proposed various methods for image stitching, including feature based, region based and deep learning based stitching algorithms. Liu *et al.* (Liu *et al.*, 2022) proposed a fast stitching method based on improved SIFT Algorithm. The feature pairs are gained by gradient normalization-based feature descriptors to improve the matching accuracy. The progressive sample consistency algorithm is applied to

eliminate the mismatch points and optimizes the transformation model in their method.

To solve the problems of high dimension of feature descriptor and low matching accuracy when the angle of rotation and angle of view is too large, Zhang *et al.* (Zhang *et al.*, 2020) raised an stitching method based on improved SURF. They establish descriptors for each feature point by Harris wavelet response and calculated simultaneously to form a new feature descriptor by the normalized gray-level difference and second-order gradient in the neighborhood. In addition, the random sample consensus (RANSAC) algorithm is used to eliminate the mismatch points. In order to improve the matching accuracy and robustness, Han *et al.* (Han *et al.*, 2018) presented a moving object detection algorithm based on binary robust invariant scalable key points (BRISK) considering the real-time and robustness requirements of detection algorithms in dynamic background. The improved BRISK algorithm is used to detect feature points. Next, the k-nearest neighbor (KNN) algorithm is applied to match feature points. Finally, the RANSAC is utilized to obtain the optimal global motion parameters.

In 2020, Wang *et al.* (Wang *et al.*, 2020) introduced an improved Harris corners extraction algorithm, which

consists of coarse screening and fine screening in the corners extraction process. Aiming at the poor matching effect, Xie *et al.* (Xie *et al.*, 2022) proposed a novel fast target recognition algorithm under the dynamic scene moving target recognition. Firstly, the template image and each frame of the video stream are processed by grayscale. Secondly, the template image and the image to be input in the video stream are processed by adaptive histogram equalization. Thirdly, the feature point descriptors of the ORB feature are quantized by the Hamming distance. Finally, the KNN algorithm is used to match and screen feature points. Peng *et al.* (Peng *et al.*, 2023) presented a novel optimal seamline detection strategy via graph cuts for HSI stitching in this work. They used robust feature matching and elastic warp to align multiple adjacent images into a common geometrical transformation. After that, they designed a novel energy function composing both the spatial and spectral information of HSI to determine an optimal seam in continuous regions with high texture consistency. Finally, the graph cuts method is used to eliminate visible artifacts. Ordóñez *et al.* (Ordóñez *et al.*, 2021) indicated a hyperspectral remote sensing image registration method based on MSER for feature detection and SIFT for feature description, which efficiently exploits the information contained in the different spectral bands to improve the image alignment.

With the deepening development of deep learning, image stitching algorithms based on deep learning are widely used. Chilukuri *et al.* (Chilukuri *et al.*, 2021) developed a robust and reliable image stitching methodology (l,r-Stitch Unit), which considers several non-homogeneous image sequences as input to generate a reliable panoramic image. The l,r-Stitch Unit further consists of a pre-processing, post-processing sub-modules and a l,r-PanoED-network. Each submodule of the method is a robust ensemble of several deep-learning, computer-vision and image-handling techniques. Zhu *et al.* (Zhu *et al.*, 2023) proposed an improved VGG16 Siamese network for the UAV remote sensing image stitching model to achieve end-to-end stitching. In their method, an improved squeeze and excitation module was introduced to effectively extract the features of the overlapping areas of the images. A network of regressing affine matrix was designed by using the LeakyReLU activation function to protect the relevant feature maps after feature fine matching, which improves the accuracy of image stitching. However, there are still issues with excessive resource and time consumption in image stitching based on deep learning at present.

Alcantarilla *et al.* (Alcantarilla *et al.*, 2012) proposed the KAZE feature which is more effective than

other feature detection algorithms. Roy *et al.* (Roy *et al.*, 2022) introduced a robust and discrimination capable hash function by considering KAZE point feature descriptor for combinatorial manipulations. The local features detected by KAZE are used to generate the hash function and this hash function not only provides a good discrimination capable value with good robustness but also shows good results for double attacks and multiple combinations of attacks.

In KAZE, nonlinear diffusion filtering is utilized to establish the scale level, which can decline speckle noise and smooth the image while preserving edge information (Fan *et al.*, 2018). In order to solve the problem of poor stitching effect and high mismatch rate caused by unclear images, an improved stitching method based on local guided KAZE and dark channel prior is proposed in this paper. The contributions of the paper are as follows: firstly, after rough matching based on KAZE features, a local fixed-point asymptotic method is introduced to optimize global objectives. This method can effectively eliminate mismatched point pairs and upgrade matching efficiency. Secondly, a compensation method based on local color and luminance difference is applied to smooth the overall image before fusing images, which can perfectly solve the problem of uneven color brightness and eliminate stitching seams. Thirdly, a dark channel prior based image defogging algorithm is introduced to enhance the foggy image and further improve the stitching effect.

This paragraph introduces the organization of the remainder of this article. Section 2 depicts the KAZE algorithm in summary. Section 3 provides the detailed introduction of the proposed stitching method in the article. Section 4 depicts the experimental results and analysis. Eventually, conclusions, shortage of the proposed method and the pending issues are indicated in Section 5.

MATERIAL

We briefly introduced the KAZE algorithm in this section. At present, the KAZE algorithm based on RANSAC is relatively popular. The process is shown in the Fig. 1.

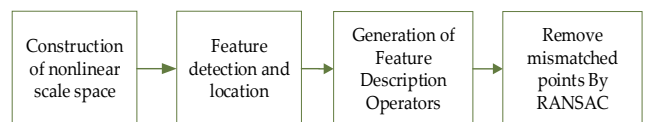


Fig. 1. The flow of KAZE algorithm based on RANSAC.

Firstly, a nonlinear scale space at maximum evolution time is constructed through variable transfer to diffusion and additive operator splitting (AOS) algorithms in the KAZE (Shen *et al.*, 2019; Jong *et al.*, 2023). The

Equation (1) provides the classic nonlinear diffusion formula.

$$\frac{\partial L}{\partial t} = \text{div}(c(x, y, t) \cdot \nabla L) \quad (1)$$

Where div and ∇ express the operations of divergence and gradient separately. In addition, $c(x, y, t)$ is the conduction function, where x and y are horizontal pixels and vertical pixels respectively, and t is the scale parameter. L represents the image luminance.

The discretization in Equation (1) in vector matrix representation can be expressed as following.

$$\frac{L^{i+1} - L^i}{\tau} = \sum_{i=1}^m A_i(L^i) L^{i+1} \quad (2)$$

Among them, A_i is the matrix which encodes the image conversion of each level and m represents the matrix dimension. L^{i+1} is gained by Equation (3).

$$L^{i+1} = (I - \tau \sum_{i=1}^m A_i L^i)^{-1} L^i \quad (3)$$

Each level of the KAZE uses the same resolution as the input image in KAZE algorithm. According to the Difference of Gaussian (DOG) pyramid model (Setumin *et al.*, 2018), each level of the DOG pyramid requires $S+2$ layers to seek the extreme value of S scales. Thus, the scale space is constructed by Equation (4).

$$\sigma(o, s) = \sigma_0 2^{o+\frac{s}{S}}, o \in [0, 1, \dots, O-1], s \in [0, 1, \dots, S+2] \quad (4)$$

Among them, σ_0 is benchmark layer scale, o means the index of the level octave and s means the index of the inner layer of the group. The scales of the key points can be calculated based on the quantity of layers within the level and the above equation.

It is important to transform the scales into evolution time in the nonlinear diffusion filtering model. Assumed that the standard deviation in the Gaussian space is σ , then the convolution can be seen as performing a duration of $t = \frac{\sigma^2}{2}$. Through a serials of evolution times, the nonlinear scale space of the whole image is attained by Equation (5).

$$L^{i+1} = [I - (t_{i+1} - t_i) \sum_{i=1}^m A_i(L^i)]^{-1} L^i \quad (5)$$

Where I means the image matrix. In feature point detection and location, KAZE feature points are gained by searching the maximum value of the normalized Hessian determinant of various scales from the local points. To meet the requirements of multi-scale feature detection, the differential operator set is normalized by Equation (6).

$$L_{\text{Hessian}} = \sigma^2 (L_{xx} L_{yy} - L_{xy}^2) \quad (6)$$

Where L_{xx} , L_{yy} and L_{xy} indicate the second order derivatives in the horizontal, vertical and cross directions respectively. The response of the detector at different scale levels is checked on a window with a size of 3×3 pixels to swiftly find out the extreme value.

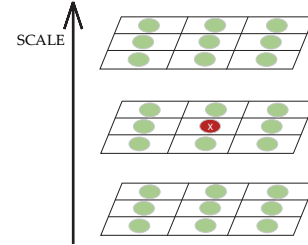


Fig.2. Extraction of feature points.

Fig. 2 shows the detection and location of feature points. Each point is paralleled with the surrounding 26 pixels. Then the extreme point which is greater than all adjacent points is selected as the key point.

After that, a window of $24\sigma_i \times 24\sigma_i$ on the gradient image centered on the feature point is selected to generate the feature description operators. The window is divided into 16 subdomains with a size of $9\sigma_i \times 9\sigma_i$ which have overlapping regions with size of $2\sigma_i$. Usually, the weight of the Gaussian kernel is set to $\sigma_1 = 2.5\sigma_i$ during calculating the subdomain description vector. The description vector of the subdomain can be obtained by Equation(7).

$$d_v = (\sum L_x, \sum L_y, \sum |L_x|, \sum |L_y|) \quad (7)$$

Then, the vector d_v of the subdomain is filtered by an unequal Gaussian kernel with a weight of $\sigma_2 = 1.5\sigma_i$. Ultimately, a vector with 64 dimensions is obtained according to normalizing.

The feature matching of KAZE algorithm is sensitive to parameter settings, which affects the matching accuracy to some extent. To avoid this issue, the RAN-SAC algorithm (Salehi *et al.*, 2022) is adopted to decline the mismatched pairs.

Firstly, Four noncollinear sample data is extracted from all detected feature pairs randomly, and the transformation matrix H can be calculated by the following:

$$s \begin{bmatrix} x' \\ y' \\ 1 \end{bmatrix} = \begin{bmatrix} h_{11} & h_{12} & h_{13} \\ h_{21} & h_{22} & h_{23} \\ h_{31} & h_{32} & h_{33} \end{bmatrix} \begin{bmatrix} x \\ y \\ 1 \end{bmatrix} \quad (8)$$

Then the model is applied for all matching pairs to acquire the number of points and the projection error until find the optimal model whose loss function is the

smallest. The loss function can be calculated by Equation (9).

$$f_{loss} = \sum_{i=1}^k \left(x_i \frac{h_{11}x_i + h_{12}y_i + h_{13}}{h_{31}x_i + h_{32}y_i + h_{33}} \right)^2 + \left(y_i \frac{h_{21}x_i + h_{22}y_i + h_{23}}{h_{31}x_i + h_{32}y_i + h_{33}} \right)^2 \quad (9)$$

It is worth noting that the number of iterations k is constantly updated. The number of iterations is determined by Equation (10).

$$k = \frac{\log(1-p)}{\log(1-\omega^m)} \quad (10)$$

Among them, p is the confidence level, ω indicates the proportion of interior points and m means the minimum value of the samples required for calculating the model.

METHODS

This section provides a detailed introduction of the proposed method. Addressing the issues of poor stitching performance and high mismatch rate for foggy images, an improved image stitching method based on local guided KAZE and dark channel prior for image enhancing is proposed in this paper. The Fig. 3 depicts the framework process of the method proposed in this article.

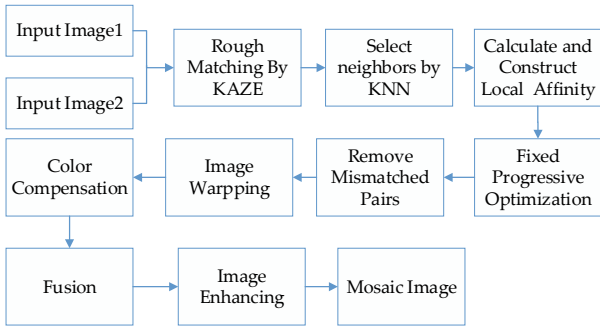


Fig.3. The framework process of the proposed method.

Since the shortcoming that KAZE feature points are usually very numerous and concentrated, we use KAZE algorithm with RANSAC for rough feature matching. Secondly, a local asymptotic optimization method is introduced to further eliminate mismatched point pairs. This step includes selecting the nearest neighbor of feature points by KNN, calculating and constructing local affine matrices, applying affine matrix asymptotic optimization to global images, and eliminating mismatched pairs. Thirdly, the warped images are obtained by the transformation matrix which is established by the remaining correct matching pairs.

Due to the differences in luminance and color of the input images, there are obvious seams in the final result. To improve the mosaic effect, we raise a compensation method which compensates the global luminance and color by calculating the difference of the luminance space and color space of overlapping area. Finally, a dark channel prior based image defogging method is applied to enhance the stitching results after fusing the distorted images. Moreover, the method proposed in this article can be used for stitching multiple images.

Rough matching

Nonlinear scale spaces are more stable which do not cause boundary blurring and detail loss. The KAZE algorithm detects feature points by constructing a nonlinear scale space, which can preserve more image details. The robustness of KAZE method is much better than other methods or blurred images caused by noise interference, weather, and other factors. However, the sensitivity of KAZE features to details is easy to cause mismatches. Therefore, we adopt the KAZE detection algorithm based on RANSAC for rough matching. Fig. 4 shows the comparison of KAZE feature matching results with other features in the absence of fog.

In the Fig. 4, (a) and (b) are the original images. (c) - (g) are the feature matching results of several comparison matching methods. Fig. 5 (h) shows the matching results of the KAZE feature matching based on RANSAC. It can be summarized that the ORB method has the most and concentrated matching pairs in clear images. However, excessive matching pairs can affect stitching efficiency to some extent.

The Fig. 5 shows the comparison results between KAZE feature matching and other feature matching in the case of fogged images. We increased the visibility to 20% fog in the original image and perform different feature matching on foggy images in the same intensity. The stitching results of different feature matching algorithms are shown in Fig. 5.

Fig. 5 (a) and Fig. 5 (b) are the input images that have been increased the visibility to 20% fog into the original images. Fig. 5 (c) - (g) represents the feature matching results of several common comparison methods corresponding to Fig. 4. Fig. 5 (h) shows the matching result of the KAZE features used in this paper. It can be seen that KAZE features can detect more matching pairs compared with other methods though image quality seriously affects feature matching results. ORB can detect the most feature pairs in clear images, but its performance is significantly inferior to KAZE in foggy image.

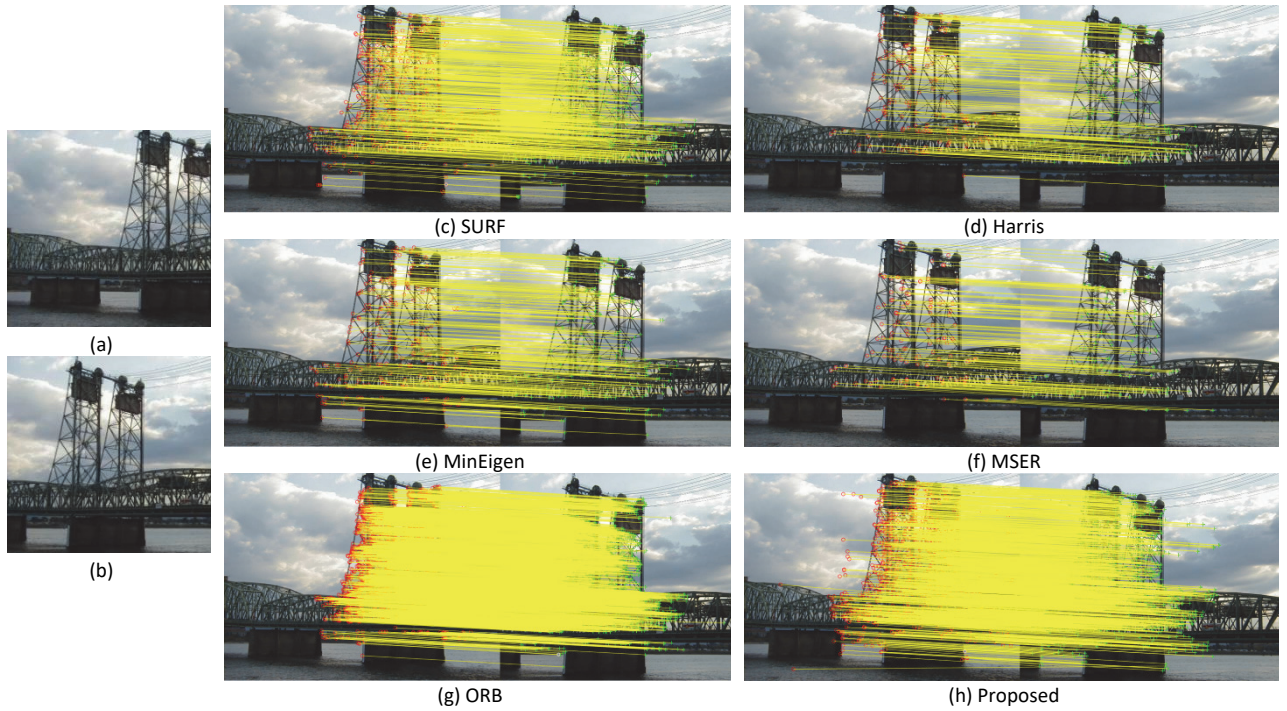


Fig.4. The comparison of KAZE feature with other features in the original images: (a) and (b) are the original images; (c) is the matching result of SURF; (d) is the matching result of Harris ; (e) is the matching result of MinEigen; (f) is the matching result of MSER; (g) is the matching result of ORB; (h) is the matching result of proposed method.

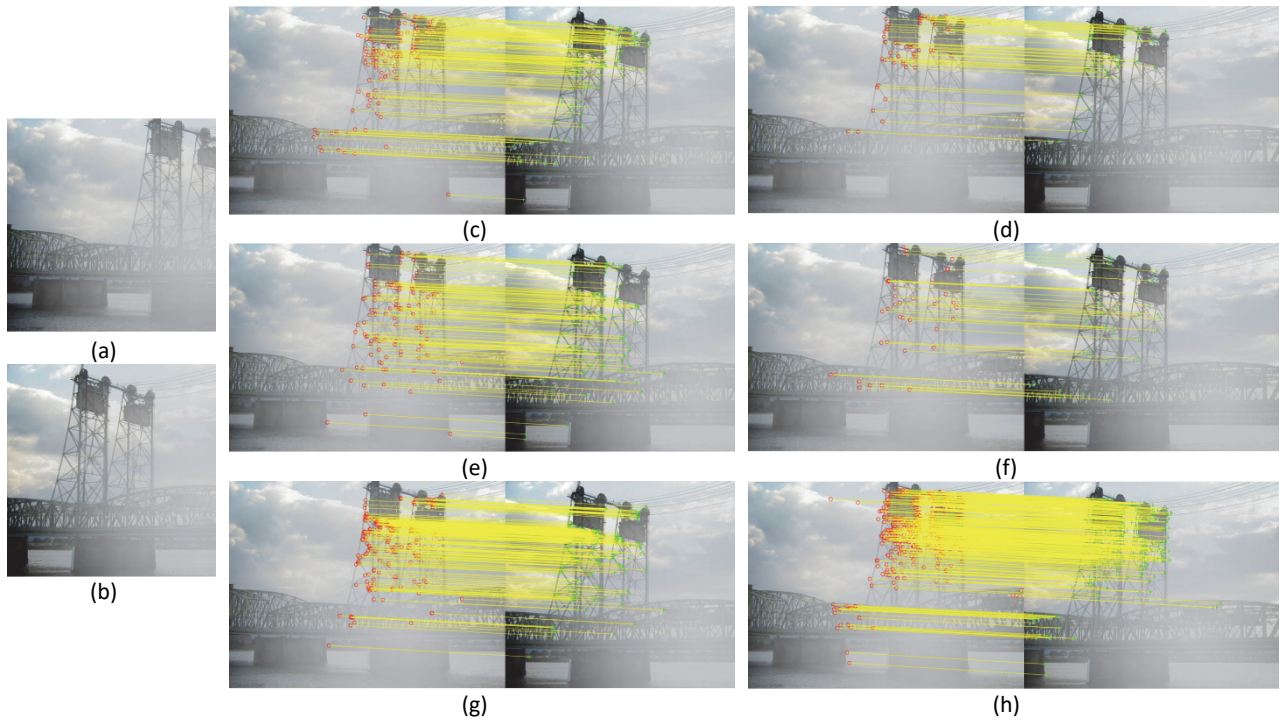


Fig.5. The comparison of KAZE feature with other features in the foggy images: (a) and (b) are the foggy images; (c) is the matching result of SURF; (d) is the matching result of Harris ; (e) is the matching result of MinEigen; (f) is the matching result of MSER; (g) is the matching result of ORB; (h) is the matching result of proposed method.

Local Progressive Optimization

Aiming at the issues of mismatch and excessive concentration of the KAZE feature pairs, a fixed point

progressive optimization solution is introduced in this paper. To ensure robustness to outlier, a set of methods for iteratively identifying other interior point sets

guided by high matching rate interior point sets are proposed, so as to obtain the best matching set.

For the N feature points obtained from rough matching, the descriptor similarity correspondence can be defined by Equation (11).

$$S = (u_j, u'_j) \quad (11)$$

where $u_j = (a_j, b_j, 1)^T$ and $u'_j = (a'_j, b'_j, 1)^T$ are the spatial homogeneous coordinates of two corresponding feature points, and j is the index of the matching pairs. To distinguish internal points from S and remove external points, the objective formula can be obtained by following:

$$y_k = \arg \max_y y^T \hat{A} x_k, y \in [0,1]^N \quad (12)$$

Where y_k is the maximum possible increase in both discrete and continuous domains. \hat{A} is a non positive definite matrix, known as a complete affinity matrix. In the continuous domain, a second order of Taylor expansion around the solution x_k of the quadratic score can be evaluated by Equation (13):

$$x^T \hat{A} x \approx x_k^T \hat{A} x_k + 2x_k^T \hat{A} (x - x_k) + (x - x_k)^T \hat{A} (x - x_k) \quad (13)$$

The last two terms of x_k can be estimated through the following equations.

$$B = x_k^T \hat{A} (y_k - x_k) \quad (14)$$

$$C = (y_k - x_k)^T \hat{A} (y_k - x_k) \quad (15)$$

The convergence condition for iteration is defined as following :

$$\frac{\|x_{k+1} - x_k\|_2}{\|x_k\|_2} < \varphi \quad (16)$$

Among them, $\| \cdot \|_2$ means the L_2 norm, and φ is a small threshold which set to 0.001 in this paper.

In order to avoid the situation that the topology of the small area in the image pair remains unchanged, multiple local affine transformations are used to approximate the image correspondence (Xia *et al.*, 2022).

We calculate the local affine transformation matrix H_i of each feature point pair. The mapping relationship of interior points (u_i, u'_i) should be consistent with the affine matrix H_i obtained from the correspondence between surrounding features. Therefore, the similarity score between corresponding relationships (u_i, u'_i) can be calculated by Equation (17).

$$S_i = \frac{2}{1 + e^{\lambda \|u'_i - H_i u_i\|_2^2}} \quad (17)$$

Where λ is a constant factor which affects the downward trend of the local affine difference $\|u'_i - H_i u_i\|_2^2$ versus the similarity score S_{ij} .

The neighbor areas of outlier in the input images may be different which almost have no common elements. The reference corresponding set R is attained by Equation (18).

$$R = (u_i, u'_i) | \frac{n_i}{K} > \varepsilon, i = 1, \dots, N \quad (18)$$

Where n_i is the number of common elements within the two K -neighborhoods of the feature points, and the ratio $\frac{n_i}{K}$ means the standard for reference points. We select four pairs of closest feature points from the reference point set R . The least square method is applied to derive the local affine matrix.

The correlation between different corresponding relationships is not only related to similarity, but also to the influence weights between them. Thus, \hat{A} can be obtained from the weight matrix W and similarity matrix C .

The non diagonal term W_{ij} is allocated as the weight of each edge $e_{ij} = (v_i, v_j)$ to quantify the impact of the tail correspondence v_j on the head correspondence v_i . The weight matrix can be obtained by follows:

$$d_{ij} = \frac{\|u_i - u_j\|_2^2}{\|\max(u) - \min(u)\|_2^2} + \frac{\|u'_i - u'_j\|_2^2}{\|\max(u') - \min(u')\|_2^2} \quad (19)$$

$$W_{ij} = \frac{2}{1 + e^{\sum_{j=1}^N d_{ij}}}, i, j = 1, \dots, N \quad (20)$$

Among them, d_{ij} deputizes the normalized distance between two corresponding relationships, and W_{ij} is the edge weight which needs to be normalized to avoid interference from image size or the number and distribution of corresponding relationships.

Given the local Affine transformation H_i , the second order edge similarity score S_{ij} can be defined as following:

$$S_{ij} = \frac{2}{1 + e^{\varepsilon (\|u'_i - u'_j\|_2^2 - \|H_i u_i - H_j u_j\|_2^2)}}, \quad (21)$$

$$i \neq j, i \in [1, N], j \in [1, N] \quad (21)$$

Among them, S_{ij} is the difference between the actual distance of two mapping points. A large value of S_{ij} indicates high affine consistency with respect to edge. The diagonal elements of the similarity matrix C is defined as Equation (22).

$$C_{ii} = S_i \quad (22)$$

Finally, The affinity matrix A is constructed as following:

$$A = W \odot C \quad (23)$$

Where \odot means the product of each element in two matrices. Obviously, the affine matrix covers the geometric consistency fraction in the global topology and is a local affine invariant, which can handle complex non rigid images.

Color difference compensation

Due to the uneven exposure and luminance of the input images, there could be obvious seams in the stitching result. In order to improve the stitching effect, we propose a mean compensation method based on local color and brightness difference. The flow chart of the compensation method is displayed in Fig. 6.

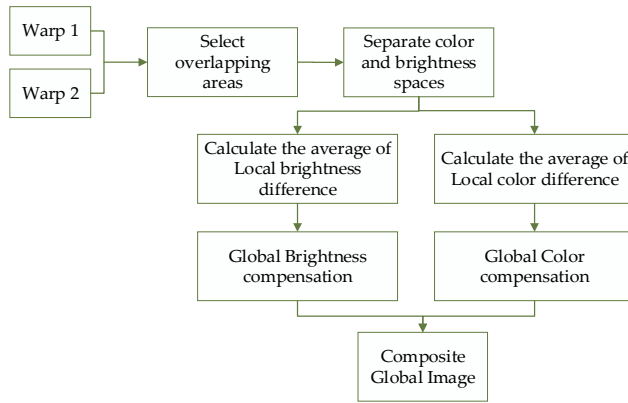


Fig.6. The flow chart of the compensation method.

Firstly, we extract the overlapping regions of warped images, which are attained by the transformation matrix in the previous step. Then, the color space and brightness space of the overlapping regions are separated to calculate the mean of the color difference and that of brightness difference respectively. The calculated means are applied to the original warped images for global brightness space compensation and global color space compensation respectively. Finally, the compensated color space and brightness space are combined into a global image. The average brightness difference and average color difference are defined as followings:

$$L_{avg} = \frac{1}{n-1} \sum_{i=1}^n (L_{i1} - L_{i2}) \quad (24)$$

$$A_{avg} = \frac{1}{n-1} \sum_{i=1}^n (A_{i1} - A_{i2}) \quad (25)$$

$$B_{avg} = \frac{1}{n-1} \sum_{i=1}^n (B_{i1} - B_{i2}) \quad (26)$$

Among them, L_{avg} is the average luminance difference. L_{i1} and L_{i2} are the luminance differences of the overlapping region of the two warped images. A_{avg}

and B_{avg} are the different average color difference. A_{i1} and B_{i1} are the two color spaces of the overlapping region of the one input image. Similarly A_{i2} and B_{i2} are two the colors of the other input image. We select the warped image with higher luminance space as the benchmark to adjust the global luminance space and



(a)



(b)

Fig.7. Original images.



(a)



(b)

Fig. 8. (a) Stitching image without compensation; (b) Stitching image with compensation.

color space of the other image. Ultimately, the compensated brightness space and color space are fused to obtain a stitching image. The two original input images are shown in Fig. 7. The Fig. 8 displays the stitching results before and after compensation.

Fig. 8 (a) shows the stitching effect without compensation, where there are obvious splicing seams in the red marked area. Fig. 8 (b) shows the splicing effect with compensation. It is easy to find that the stitching result after compensation are smoother and more even. It is sufficient to prove the effectiveness of compensation.

Image enhancing based on dark channel prior

There are some pixels in most images, which have a low value in a channel (Kokul *et al.*, 2020). If a image is represented by J , the dark channel of the image J^D can be represented as:

$$J^D = \min_{C \in \{r,g,b\}} (\min_{y \in M(x)} (J^C(y))) \quad (27)$$

Where $M(x)$ represents a square window centered on pixel x , and J^C means the dark primary colors of the three channels of the fog free image. The dark channel is obtained by performing minimal filtering on the original image. The dark channel of the image without fog except for the sky area tends to zero (He *et al.*, 2010).

After extracting the dark channel, the brightness of the dark channel in the image is used to estimate the overall atmospheric light intensity. The transmittance can be calculated by the deformation of the atmospheric scattering model.

$$\frac{I^c(x)}{A^c} = t(x) \cdot \frac{J^c(x)}{A^c} + (1 - t(x)) \quad (28)$$

Among them, represents the observed intensity, A means the global atmospheric light, and $t(x)$ is the medium transmission which is a constant. Two minimum filters are performed on both ends of the above equation. The first filter takes the minimum values for the three channels R, G, and B at both ends of the equation. The second filter takes the minimum pixel in a square area centered on the target pixel. This process is described in Equation (29).

$$\min_{y \in M(x)} \left(\min_{C \in \{r,g,b\}} \frac{I^C(x)}{A^C} \right) = t'(x) \cdot \min_{y \in M(x)} \left(\min_{C \in \{r,g,b\}} \frac{J^C(x)}{A^C} \right) + (1 - t'(x)) \quad (29)$$

Then, the transmittance is defined as following:

$$t'(x) = 1 - \min_{y \in M(x)} \left(\min_{C \in \{r,g,b\}} \frac{I^C(x)}{A^C} \right) \quad (30)$$

To make the processing results look more natural, we choose to retain a portion of the fog that covers the distant view. The parameter of defogging intensity μ is introduced and the corrected transmittance is adjusted as following:

$$t(x) = 1 - \mu \cdot \min_{y \in M(x)} \left(\min_{C \in \{r,g,b\}} \frac{I^C(x)}{A^C} \right) \quad (31)$$

After obtaining the transmittance map, the brightness of the scene can be restored according to the haze model formula. Finally, $J(x)$ is represented as Equation (32).

$$J(x) = \frac{I(x) - A}{\max(t(x), t_0)} + A \quad (32)$$

Where t_0 represents the lower limit value of atmospheric transmittance, which is taken as 0.1 in this paper. Due to the fact that the brightness of the scene is usually not as bright as that in the atmosphere, an exposure processing is applied to adjust the brightness of the image. Finally, the restored enhanced image can be obtained by calculating the R, G, and B channels of the image separately. The process of image enhancing is shown as Algorithm 1.

Algorithm 1: Enhancing Algorithm

Input: The foggy image and the parameter of defogging intensity μ .

Output: The enhancing image.

- 1: Calculate the minimum pixel value of the input image and locate the dark channel.
 - 2: Finding the brightest pixel point in dark channel for estimating atmospheric light intensity.
 - 3: Divide the image into N blocks.
 - 4: Repeat:
 - 5: Calculate the ratio of each pixel point to atmospheric light intensity the transmission rate in each block by Equation (28).
 - 6: Calculate the transmittance according to Equation (31).
 - 4: Until all the transmittance of N blocks are calculated.
 - 5: Defog and reconstruct R, G, and B channels to obtain defogging image images by Equation (32).
-

RESULTS

In this section, we conduct experiments on two databases using different stitching algorithms to verify the effectiveness of the proposed method in this paper. The two databases in this paper are from the USI SIPI database of the University of Southern California (Mahto *et al.*, 2022)

and Ground truth database of the University of Washington (Brostow *et al.*, 2009) separately. Both databases are open source for image processing. The USI SIPI image database covers different types of images, such as antenna images, texture images, composite images and sequence images. The images in USI SIPI image database are mainly used for research purposes. The Ground truth database contains high quality and high resolution images, which designates extended duration digital lenses to those who have research on ego-motion or driving scenarios images. The emergence of this database meets the evaluation of image related algorithms. Furthermore, all of the experiments in this paper are run in the Matlab 2022b.

To comprehensively evaluate the proposed method, we contrast it with other currently popular methods in terms of intuitive renderings and quantitative assessment.

Intuitive effect

We take two images from the Ground truth Database as examples to compare the matching pairs and stitching results of the proposed method with those in other popular stitching methods. The original images are revealed in Fig. 9. Table 1 shows the comparison stitching results.



Fig. 9. *Original Images*.

The image in bottom right corner of each row represents the enlarged display of the red selected region in Table 1. On the one hand, there are obvious mismatches in the matching results of SURF algorithm. Harris, BRISK, and MSER detected fewer matching pairs. The proposed method not only detects more matching pairs, but also has higher matching accuracy. On the other hand, it is easy to discover that the proposed stitching method provides clearer details for stitching images without ghosting. The blue area in the table indicates that the proposed method preserves the details of the image well with higher contrast. The other comparison methods cannot reflect clear details.

In order to further demonstrate the robustness of the proposed algorithm in this paper, we also add a 20% visibility fog to the original image for comparative experiments of stitching. The Foggy image are displayed in Fig. 10. Table 2 shows the comparison stitching results of foggy images.



Fig. 10. *Foggy Images*.

Among them, Brisk and Harris were unable splice due to the inability to detect matching pairs. Moreover, it is impossible to splice due to less than four matching pairs detected by MSER. In Table 2, the matching pairs detected by other comparison algorithms are relatively few and the splicing results are not clear. It is obvious that the proposed method in this paper can still detect a large number of matching pairs in foggy images. Furthermore, the proposed algorithm has a clearer stitching effect due to image enhancement processing.

Quantitative evaluation

So as to comprehensively assess the availability of the proposed method, we conducted a quantitative evaluation in terms of the quantity of feature matching pairs, RMSE, MAE and processing time (Khajezadeh *et al.*, 2022; Qi *et al.*, 2020).

We randomly select eight sets of images from the databases previously mentioned and perform fuzzy processing to a certain extent. The results of several matching methods on the original images and blurred images are revealed in Table 3

It is easy to observed from Table 3 that both the proposed method and ORB algorithm can detect abundant matching pairs for the original image. But for foggy images, the proposed method can still detect a large number of matching pairs. Other methods sometimes fail to detect matching pairs when matching foggy images.

In order to sufficiently validate the effectiveness of the proposed algorithm, we compared it with other algorithms in terms of RMSE and MAE. For two input images I_1 and I_2 , RMSE and MAE are calculated by follows:

$$RMSE(I_1, I_2) = \sqrt{\frac{1}{N} \sum_{i=1}^N (p_{i1} - p_{i2})^2} \quad (33)$$

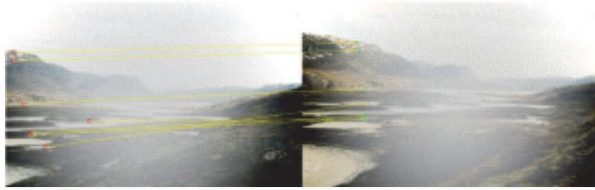
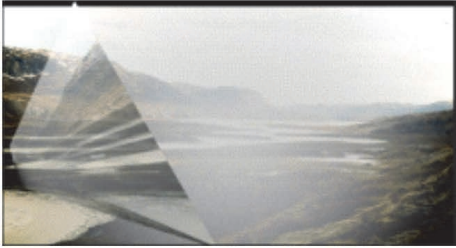
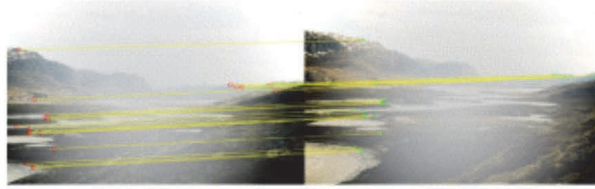

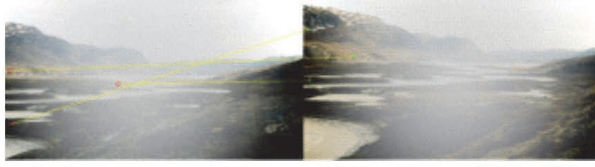
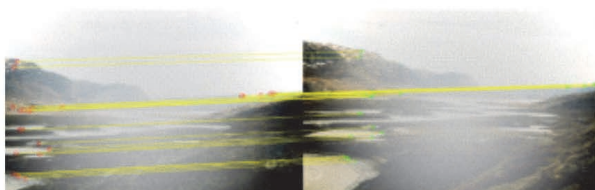



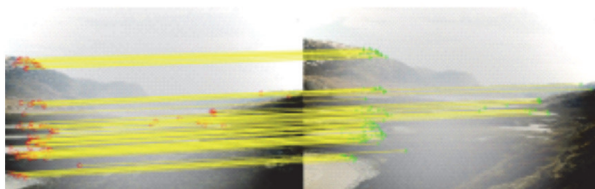

$$MAE(I_1, I_2) = \frac{1}{N} \sum_{i=1}^N |p_{i1} - p_{i2}| \quad (34)$$

Among them, N is the number of the matching pairs p_{i1} , p_{i1} and p_{i2} are the matching points in the two input images respectively. Table 4 lists the results of MAE and RMSE using the above eight group images for several different algorithms.

Table 1. The comparison results of different stitching method in original images.

Methods	Match Figure	Stitching Image
SURF[9]		
Harris [14]		
BRISK [11]		
MinEigen		
MSER [13]		
SIFT		
ORB[12]		
Our method		

Table 2. The comparison results of different stitching method in foggy images.

Methods	Match Figure	Stitching Image
SURF		
MinEigen		
MSER		Unable to splice due to insufficient matching pairs
SIFT		
ORB		
Our method		

In Table 4, BRISK and Harris methods cannot calculate MAE and RMSE values due to the lack of feature matching point pairs. The MinEigen algorithm performs well in RMSE and MAE values in some datasets. In most cases, the RMSE and the MAE of the proposed method in this paper perform better than other comparison methods.

Additionally, the processing time of the different stitching methods are also compared in this paper. The comparison results are displayed in Table 5.

It is obvious to observe that stitching based on SURF is comparatively time-saving. The processing time of ORB based splicing method is the longest.

Table 3. The comparison of the number of matching pairs on the different methods.

Data	Type	SURF	BRISK	MSER	MinEigen	Harris	ORB	Proposed
Data1	Org	69	14	20	32	19	101	667
	Fog	11	0	4	6	3	2	114
Data2	Org	123	71	19	68	36	321	769
	Fog	20	4	1	21	6	8	129
Data3	Org	205	109	51	125	87	771	912
	Fog	14	3	11	38	35	27	198
Data4	Org	474	231	135	232	157	2348	1888
	Fog	119	32	38	107	52	227	495
Data5	Org	247	63	38	389	317	3440	4354
	Fog	45	7	19	87	31	67	1322
Data6	Org	327	94	34	366	277	3575	3440
	Fog	21	6	4	53	8	32	262
Data7	Org	354	82	45	180	136	832	2662
	Fog	31	5	2	35	3	21	720
Data8	Org	151	22	18	81	43	223	694
	Fog	7	0	3	19	0	6	181

Table 4. The comparison of MAE and RMSE of different methods.

Data	Estimate	SURF	BRISK	MSER	MinEigen	Harris	ORB	Proposed
Data1	MAE	0.4196	-	0.0585	0.1816	0.3854	0.3969	0.2062
	RMSE	0.4419	-	0.0773	0.1933	0.4159	0.4293	0.2693
Data2	MAE	0.0796	0.0702	0.0989	0.075	0.0831	0.1014	0.0972
	RMSE	0.0954	0.0973	0.1324	0.1021	0.0951	0.1261	0.1226
Data3	MAE	0.1769	0.1356	0.1273	0.1193	0.1245	0.1275	0.1086
	RMSE	0.1936	0.1701	0.1615	0.1533	0.1503	0.1526	0.1139
Data4	MAE	0.1083	0.0747	0.0861	0.0867	0.0843	0.0887	0.0856
	RMSE	0.1655	0.1067	0.1027	0.1186	0.1042	0.1240	0.1116
Data5	MAE	0.0828	0.0818	0.0931	0.0600	0.0795	0.0711	0.0393
	RMSE	0.1021	0.1024	0.116	0.0798	0.0948	0.0883	0.0522
Data6	MAE	0.1833	0.0926	0.1652	0.1434	0.1297	0.1109	0.0915
	RMSE	0.1938	0.1173	0.2016	0.1833	0.1570	0.1316	0.1167
Data7	MAE	0.0823	0.0881	0.0794	0.0598	0.0812	0.0710	0.0778
	RMSE	0.1225	0.1307	0.1095	0.0801	0.1207	0.1038	0.0977
Data8	MAE	0.1376	-	0.1503	0.0870	-	0.0951	0.1487
	RMSE	0.1791	-	0.2013	0.1048	-	0.1253	0.1931

The processing time of the proposed method in this paper is relatively stable and short.

Overall, the method proposed in this paper outperforms other methods in four aspects: number of matching

pairs, RMSE, MAE and processing time. Moreover, the proposed method in this article can be applied to both clear and foggy images. The stitching effect of the proposed method performs much better than other comparison algorithms especially for blurry images.

Table 5. Comparison of the processing time of different methods.

Data	SURF	BRISK	MSER	MinEigen	Harris	ORB	Proposed
Data1	0.4337s	-	0.5232s	0.4907s	0.4429s	0.4469s	0.4202s
Data2	0.4429s	0.5473s	0.5198s	0.5022s	0.5106s	0.5235s	0.5019s
Data3	0.3320s	0.4529s	0.3371s	0.3765s	0.3760s	0.3522s	0.4047s
Data4	0.3334s	0.4517s	0.3673s	0.3908s	0.5600s	0.5355s	0.4490s
Data5	0.7292s	0.7922s	0.7099s	1.0055s	0.7312s	0.9640s	0.8270s
Data6	0.6903s	0.8045s	0.6880s	0.7274s	0.7280s	1.0415s	0.6770s
Data7	0.7441s	0.8564s	0.7927s	0.8829s	0.8153s	1.0203s	0.7365s
Data8	0.6897s	-	0.6737s	0.8282s	-	0.8322s	0.6458s

DISCUSSION AND CONCLUSION

In this article, an improved stitching method based on local guided KAZE and dark channel prior for image enhancing is proposed. Firstly, the KAZE feature with RANSAC is utilized for feature coarse matching. Secondly, a local fixed point asymptotic method is introduced to optimize the global objective and eliminate mismatched pairs. Then, the transformation matrix for the remaining matching point pairs is estimated. Thirdly, color space and luminance space compensation are raised to the concatenated images to improve the unevenness of the warped images. Aiming at the problem of poor blurry image stitching effect, a dark channel prior image defogging algorithm for post-processing is applied to obtain the excellent result.

The proposed method in this article has been tested on images from both USI SIPI database and Ground truth database, and compared with several popular stitching algorithms in terms of visual effects and quantitative value. The experimental results indicate that the proposed algorithm outperforms other methods in terms of visual effect, number of feature point matching, RMSE, MAE and processing time. Furthermore, the

proposed stitching method can achieve smoother and more detailed stitching images especially for blurred images.

The proposed method can be applied for multiple areas, such as drone panoramic stitching and criminal reconnaissance. Nevertheless, in situations such as high-rise buildings with significant changes in perspective where the disparity is particularly large, the stitching effect of the proposed method cannot be accurately aligned. In future work, we will continue to explore stitching under such large parallax conditions and optimize under other challenging conditions such as low light, motion blur, or glare. In addition, due to the rapid development of deep learning, we will combine feature registration research based on deep learning to optimize the extraction of image features as future work.

ACKNOWLEDGEMENTS

This work was supported in part by the Youth Foundation of Jilin Province (No.62205332) and the National Natural Science Foundation of China (Grant No.62405310).

REFERENCES

- Aubert G, Aujol JF (2008). A variational approach to removing multiplicative noise. *SIAM J Appl Math* 68: 925–46.
- Alcantarilla PF, Bartoli A, Davison AJ (2012). KAZE features. *Lect Notes Comput Sci* 7584:214–27.
- Brostow GJ, Fauqueur J, Cipolla R (2009). Semantic object classes in video: A high-definition ground truth database. *Pattern Recogn Lett* 30(2): 88–97.
- Chilukuri PK, Padala P, Padala P, Desanamukula VS, Pvgd PR (2021). L, r-stitch unit: encoder-decoder-cnn based image-mosaicing mechanism for stitching non-homogeneous image sequences. *IEEE Access* 9, 16761–82.
- Fan J, Wu Y, Li M, Liang W, Cao Y (2018). SAR and optical image registration using nonlinear diffusion and phase congruency structural descriptor. *IEEE T Geosci Remote* 56(9), 5368–79.
- Gómez-Reyes JK, Benítez-Rangel JP, Morales-Hernández LA (2022). Image Mosaicing Applied on UAVs Survey. *Appl Mech Mater* 12(5), 2729.
- Han LL, Wang SM, Li WJ (2018). Moving object detection based on BRISK feature in dynamic background. *P Soc Photo-Opt Ins.*

- He K, Sun J, Tang X (2010). Single image haze removal using dark channel prior. *IEEE T Pattern Anal* 33(12): 2341-53.
- Jong, T.K.; Bong, D.B.L (2023). An effective feature detection approach for image stitching of near-uniform scenes. *Signal Process* 110: 116872.
- Khajehzadeh M, Taha MR, Keawsawasvong S (2022). An effective artificial intelligence approach for slope stability evaluation. *IEEE Access* 10: 5660-71.
- Kokul T, Anparasy S (2020). Single Image Defogging using Depth Estimation and Scene-Specific Dark Channel Prior. *Proc CVPR IEEE* 190-5.
- Lin M, Liu T, Li Y, Miao X, He C (2022). Image stitching by disparity-guided multi-plane alignment. *Signal Process* 197: 108534.
- Liu Y, He M, Wang Y, Sun Y, Gao X (2022). Farmland aerial images fast-stitching method and application based on improved sift algorithm. *IEEE Access* 10: 95411-24.
- Mahto DK, Anand A, Singh AK (2022). Hybrid optimisation-based robust watermarking using denoising convolutional neural network. *Soft Comput* 1-12.
- Nie L, Lin C, Liao K (2022). Learning edge-preserved image stitching from multi-scale deep homography. *Neurocomputing* 491: 533-43.
- Ordóñez Á, Acción Á, Argüell F; Heras, D. B (2021). HSI-MSER: Hyperspectral Image Registration Algorithm Based on MSER and SIFT. *IEEE J Sel Top Appl* 14: 12061-72.
- Peng Z, Ma Y, Zhang Y (2023). Seamless UAV hyperspectral image stitching using optimal seamline detection via graph cuts. *IEEE T Geosci Remote*.
- Pham NT, Park S, Park CS (2021). Fast and efficient method for large-scale aerial image stitching. *IEEE Access* 9: 127852-65.
- Qi J, Du J, Siniscalchi SM (2020). On mean absolute error for deep neural network based vector-to-vector regression. *IEEE Signal Proc Let* 27: 1485-9.
- Roy M, Thounaojam DM, Pal S (2022). Perceptual hashing scheme using KAZE feature descriptors for combinatorial manipulations. *P Soc Photo-Opt Ins* 81(20): 29045-73.
- Salehi B, Jarahizadeh S, Sarafraz A (2022). An improved RANSAC outlier rejection method for UAV-derived point cloud. *Remote Sens-Basel* 14(19): 4917.
- Setumin S, Suandi SA (2018). Difference of Gaussian oriented gradient histogram for face sketch to photo matching. *IEEE Access* 6: 39344-52.
- Shen Y, Peng F, Zhang Z (2019). Efficient optical proximity correction based on semi-implicit additive operator splitting. *Opt Express* 27(2): 1520-28.
- Wan Q, Chen J, Luo L, Gong W, Wei L (2021). Drone Image Stitching Using Local Mesh-Based Bundle Adjustment and Shape-Preserving Transform. *IEEE T Geosci Remote* 59(8): 7027-37.
- Wang Z, Yang Z (2020). Review on image-stitching techniques. *P Soc Photo-Opt Ins.* 26: 413-30.
- Wang Z, Zhang S, Fang Z, Wang W, Zhang C, Yang G (2020). Image Stitching Algorithm Based on Improved Harris Corners Extraction. *IEEE* 714-18.
- Xia Y, Ma J (2022). Locality-Guided Global-Preserving Optimization for Robust Feature Matching. *IEEE T Image Process* 31: 5093-108.
- Xie Y, Wang Q, Chang Y, Zhang X (2022). Fast target recognition based on improved ORB feature. *Appl Mech Mater* 12(2): 786.
- Zhang L, Huang H (2022). Image Stitching with Manifold Optimization. *IEEE T Multimedia*.
- Zhang T, Zhao R, Chen Z (2020). Application of migration image registration algorithm based on improved SURF in remote sensing image mosaic. *IEEE Access* 8: 163637-45.
- Zhu F, Li J, Zhu B (2023). Uav remote sensing image stitching via improved vgg16 siamese feature extraction network. *Expert Syst Appl* 229: 120525.